The free vibrations analysis of the cupula in the inner ear using a natural neighbor meshless method

Carla F. Santos[a,*], J. Belinha[a,b,**], Fernanda Gentil[c], Marco Parente[a,b], Renato Natal Jorge[a,b]

[a] *INEGI, Institute of Mechanical Engineering and Industrial Management, Rua Dr. Roberto Frias, 400, 4200-465 Porto, Portugal*
[b] *Faculty of Engineering of the University of Porto, FEUP, Rua Dr. Roberto Frias, 4200-465 Porto, Portugal*
[c] *Clínica ORL-Dr. Eurico Almeida, Widex, Escola Superior de Saúde–I.P. Porto, Porto, Portugal*

Keywords:
Meshless methods
NNRPIM
Inner ear
Free vibrations
Cupula

A B S T R A C T

The cupula is a part of the inner ear semi-circular canals that plays an important role in the maintenance of the human balance. In order to understand the dynamic response of the cupula, first it is necessary to obtain its vibration frequencies. A two-dimensional and three-dimensional geometrical model of the cupula was built. Then, a free vibration analysis was performed using two distinct numerical techniques, the finite element method (FEM) and the natural neighbor radial point interpolation method (NNRPIM). Besides the fundamental analysis, other scenarios were studied, aiming to analyze the environment of the cupula (in healthy and pathologic scenarios). The results obtained with the geometrical models show that NNRPIM is capable to deliver results very close with the FEM. Additionally, the NNRPIM formulation possesses a high convergence and acceptable computational costs.

This work presents for the first time a computational study on the free vibration analysis of the cupula and shows an alternative numerical technique to calculate with precision the natural frequency of the cupula. The outcomes of this work will allow the development of alternative therapies for cupulolithiasis, which causes severe dizziness.

1. Introduction

The vestibular system of the inner ear is the least studied part of the human ear; however, this is the main responsible for the balance function of the human body. When this system fails, the symptoms lead to intense dizziness most of the times. Several mathematical models have been made through the years to represent some parts of the vestibular system [1–5]. The computational simulation of such distinct structures is performed using numerical methods. Today, the preferential numerical method used is the FEM [6] and the most commonly used finite elements are the linear formulation elements, which assume triangle or quadrilaterals shapes for 2D analyses and tetrahedron or hexahedron shapes for 3D analyses [6].

Nowadays, using the computed axial tomography (CAT) imaging technique, it is virtually possible to construct the geometric model of any bio-structure of the human body. Afterward, in order to create a finite element mesh, this geometrical model can be discretized using triangles or quadrilateral elements (2D analyses) or using tetrahedrons or hexahedrons elements (3D analyses). However, this discretization technique could represent a heavy pre-processing cost, especially if a uniform mesh is intended. Additionally, the model's mesh quality strongly affects the FEM performance, and any mesh refinement during the analysis represents an additional computational cost.

Fortunately, in the last decades, meshless methods [7] have been under strong development and are continuously extending their application field. Today, these more flexible discretization techniques are a competitive and alternative numerical method in computational mechanical analysis, due to the efficiency and accuracy of their discretization formulation [8].

The meshless methods discretize the domain based in a cloud of nodes [7–11], instead of the rigid element concept used in FEM. In the early years, the solution of partial differential equations was the main focus of interest [8]. However, today, meshless methods are applied to a wide-range of applications [10].

Meshless methods can be divided into many classes or even subclasses; one of the most common classification used is the "not-truly meshless methods" or "truly meshless methods" classification [10].

A meshless method is labeled "not-truly" when a background mesh is required to perform the numerical integration of the integro-differential equations ruling the studied physical phenomenon.

On the other hand, "truly" meshless methods only require an unstructured cloud of nodes to discretize the problem domain. Because the influence domain, integration points, shape functions and other necessary mathematical constructions are obtained directly from the spatial coordinates of the nodes.

Thus, truly meshless methods [10,12–16] are capable to obtain the cloud of nodes using just CAT scan or the MRI images by considering the pixels (or voxels) position. Afterward, using only the nodal spatial information, these truly meshless methods are able to obtain directly the nodal connectivity, the integration points and the shape functions [10]. Furthermore, using the gray range of medical images, truly meshless methods are even capable of recognizing distinct biological structures and then attribute to each node the corresponding material properties [10].

The meshless methods already proved to possess clear advantages over other numerical techniques and to be a reliable option in biomechanics computational applications [17], particularly when combined with medical imaging techniques (CAT scan and MRI) [18,19].

In the literature it is possible to find several research works showing the efficiency of meshless methods in several demanding fields, such as the prediction of crack propagation [20], the analysis of plates assuming functionally graded materials [21] or piezoelectric materials [22] or plate materials damaged by cracks [23]. Regarding the solution requiring the determination of eigen-values and eigen-vectors, meshless methods were efficiently extended to buckling studies [24,25,26] and free vibrations analysis [27,28,29]. Additionally, the literature shows that the structural dynamic analysis assuming truly meshless methods was successfully performed [30].

One of the advantage of meshless methods over FEM are the remeshing efficiency, which in biomechanics structures could be crucial to the final result [31,32].

Thus, due to their formulation, meshless methods allow to introduce or remove nodes from the problem domain without disturbing significantly the final solution. In biomechanics this feature reveals itself to be an advantage because soft tissues (such as muscles, tendons, extra cellular matrix, etc.) and bio-fluids present very large deformations. Therefore, external actions applied to the solid will lead to highly distorted final configurations. If the problem domain is discretized with elements, possibly the final geometry of the elements will be incompatible, leading to the loss of accuracy. In this case, the solution is to create a new element mesh discretizing the geometry of the final configuration. This is an inefficient and time consuming step. Alternatively, in meshless methods there is no pre-established nodal connectivity. Thus, using the concept of influence-domain and the final nodal distribution configuration (naturally adapted to the geometry of the final configuration) a new nodal connectivity will be established, without requiring a new domain remeshing. Additionally, if the nodal discretization is highly distorted, new nodes can be added to the domain to improve the discretization and then the influence-domain concept will allow to enforce the nodal connectivity [10].

Meshless methods have been used to simulate body fluids with low velocities, such as the vestibular system [33,34]. These works apply the smoothed particle hydrodynamics (SPH) technique to capture the fluid/solid interaction occurring between the endolymph and the cupula and otoconia (a highly demanding topic in computational mechanics).

Nevertheless, the main topic of this work is not the study of those fluid/solid interactions but the pioneer analysis of the free vibration of the cupula – a fundamental part of the vestibular system.

At the author's best knowledge, this is the first research work studying the free vibration analysis of the cupula. The main objective of this manuscript is to obtain the natural frequencies of the cupula (both in 2D and 3D) with and without attached otoconia particles. The obtained results will allow to understand the magnitude of the natural frequency of the cupula, allowing to design in the future new therapies to minimize the effects of vertigo.

The numerical analysis is performed using an improved meshless method [12,35],—the NNRPIM—and the FEM (for comparison purposes). Notice that the FEM formulations is well described in the literature, in which several handbooks can be found [6]. The NNRPIM is a truly meshless method [10], which means that it is capable to fully and accurately discretize the problem domain using as information only a micro-CT scan. This is an advantage, since NNRPIM allows to discretize the problem domain using only the nodal cloud coming from the voxel position of the micro-CT scan (no other information is required). Then, using the natural neighbor concept, the Voronoï diagram discretizing the problem domain can be constructed. From the Voronoï diagram it is possible to establish directly the nodal connectivity and define the position and weight of background integration points. The NNRPIM formulation and its extension to free vibration analysis will be described with detailed in the next sections. Afterward, the results obtained from the cupula model will be presented and discussed.

2. Nodal connectivity and shape function of natural neighbors

The natural neighbors concept was used for the first time by Sibson for data fitting and smoothing [36,37]. There are two dual mathematical tools used in the determination of the natural neighbors: the Voronoï diagrams [38] and the Delaunay triangulation [39].

Generally, in meshless methods, the nodal connectivity is enforced by the influence-domain concept, in which nodes are searched within a fixed area (in the case of a 2D problem) or a fixed volume (in the 3D problems). Due to its simplicity, several meshless methods use this concept [40–43].

Alternatively, the connectivity between nodes in the NNRPIM is imposed by the "influence-cells" created by the Voronoï diagram [12]. The influence domain formed by n nodes, contribute to the interpolation of the interest point $\boldsymbol{x}_I$ (Fig. 1a) belonging to the problem domain, $\Omega \in \mathbb{R}^3$. There are two types of influence domains, the "First degree influence-cell" and the "Second degree influence-cell". In the first case, an interest point $\boldsymbol{x}_I \in \Omega$ searches for its natural neighbor nodes following the natural neighbors from the Voronoï construction, the second one goes further and add to the cell also the natural neighbor nodes of the first ones. More details can be found in [10].

Regarding the distribution of the background integration points, the NNRPIM uses the Voronoï diagram to define the background distribution of integration points required to integrate the integro-differential equations governing the physical phenomenon. As Fig. 1b shows, following the Delaunay triangulation [10], each Voronoï cell can be divided into quadrilaterals. Then, each quadrilateral sub-cell (Fig. 1c) can be filled with integration points using the Gauss–Legendre quadrature scheme. Previous studies showed that the NNRPIM integration scheme allows to obtain better results than other integration schemes [44].

Notice that the NNRPIM integration scheme is in fact a nodal integration scheme. In the literature it is possible to find several other efficient nodal integration schemes, such as the one combined with the boundary element method [45], or the adaptative integration scheme presented in [46], or the conforming nodal integration scheme proposed in [47].

The NNRPIM uses the radial point interpolators to construct its shape functions. Thus, consider a function $f(\boldsymbol{x}_I)$ defined in the domain Ω_I, which is discretized by a set of n nodes. Notice that $\Omega_I \subset \Omega$ and represent the physical domain of the influence-cell. The interpolation function $f(\boldsymbol{x}_I)$, using the NNRPIM, passes through all nodes in the domain Ω_I, using a radial basis function (RBF) and a polynomial basis function. Assuming that $f(\boldsymbol{x}_I)$ is just affected by the n nodes within the influence-cell of the point of interest $\boldsymbol{x}_I = \{x_I, y_I\}^T$. The value of function $f(\boldsymbol{x}_I)$ at the point of interest $\boldsymbol{x}_I$ is obtained by,

$$f(\boldsymbol{x}_I) = \sum_{i=1}^{n} R_i(\boldsymbol{x}_I) a_i(\boldsymbol{x}_I) + \sum_{j=1}^{m} p_j(\boldsymbol{x}_1) b_j(\boldsymbol{x}_1), = \{\mathbf{R}^T(\boldsymbol{x}_I), \boldsymbol{p}^T(\boldsymbol{x}_1)\} \begin{Bmatrix} a \\ b \end{Bmatrix}, \tag{1}$$

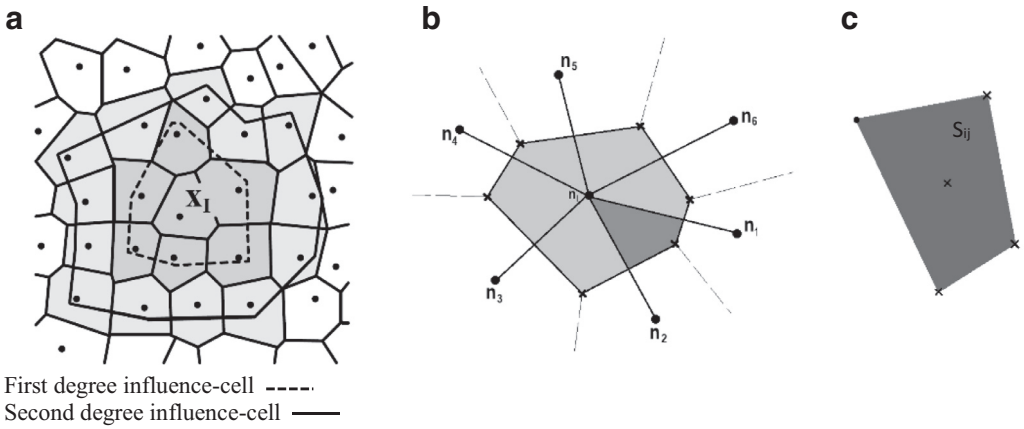

Fig. 1. (a) Influence-cells representation; (b) Voronoï cells; (c) generated quadrilateral.

where $R_i(\boldsymbol{x}_I)$ is the RBF, n is the number of nodes in the influence-cell of $\boldsymbol{x}_I$. The coefficients $a_i(\boldsymbol{x}_I)$ and $b_j(\boldsymbol{x}_I)$ are the non-constant coefficients of $R_i(\boldsymbol{x}_I)$ and $p_j(\boldsymbol{x}_I)$, respectively. The monomials of the polynomial basis are defined by $p_j(\boldsymbol{x}_I)$ and m is the basis monomial number. The variable r_{ij} is the distance between the relevant node $\boldsymbol{x}_i = \{x_i, y_i\}^T$ and the neighbor node $\boldsymbol{x}_j = \{x_j, y_j\}^T$, $r_{ij} = \sqrt{(x_j - x_i)^2 + (y_j - y_i)^2}$. Several known RBFs are well studied and developed in [48,49]. This work uses the Multiquadric (MQ) function $R(r_{ij}) = (r_{ij}^2 + c^2)^p$, proposed initially by Hardy [50], where c and p are two parameters that need to be optimized, since they affect the performance of the RBFs.

Notice that each integration weight should possesses its own c parameter. Thus, for integration point I with an integration weight $\hat{\omega}_I$, the shape parameter c is obtained with: $c_I \cong \gamma\hat{\omega}_I$. This spatial dependence of the RBF's shape parameter is demonstrated in research works available in the literature [10,12]. Previous works on the NNRPIM found that parameter γ should be close to zero, $\gamma \cong 0$, and p should be close to one, $p \cong 1$ [10]. However, these values cannot be $\gamma = 0$ and $p = 1$. The use of the exact integer value for p leads to a singular moment matrix and assuming a null γ leads to singular moment matrix [10]. Furthermore, previous works [10,12] have shown that values of p very close to the unit allow to obtain the most accurate solutions (regardless the analyzed problem). Thus, the authors have decided to use $p = 1.0001$ or $p = 0.9999$. Additionally, as shown in [10], the parameter γ should be very close to zero, because as its value grows, the RPI shape functions lose its interpolation properties. Thus, the authors have selected $\gamma = 0.0001$ in order to "maximize" the RPI interpolation properties. Nevertheless, optimizing the RBF shape parameters is a never-ending research topic [10].

Commonly, the polynomial basis has to possess a low degree to guarantee that the interpolation matrix of RBF is invertible [10]. Thus, in this work the constant polynomial basis is used. Nevertheless, it is possible to include in the formulation several distinct (complete) polynomial basis,

$$\text{Absence of Basis } \mathbf{x}^{\mathrm{T}} = \{x, y\};\ \boldsymbol{p}^T(\boldsymbol{x}) = \{0\};\ m = 0, \tag{2}$$

$$\text{Constant Basis } \boldsymbol{x}^{\mathrm{T}} = \{x, y\};\ \boldsymbol{p}^T(\boldsymbol{x}) = \{1\};\ m = 1, \tag{3}$$

$$\text{Linear Basis } \boldsymbol{x}^{\mathrm{T}} = \{x, y\};\ \boldsymbol{p}^T(\boldsymbol{x}) = \{1, x, y\};\ m = 3, \tag{4}$$

$$\text{Quadratic Basis } \boldsymbol{x}^{\mathrm{T}} = \{x, y\};\ \boldsymbol{p}^T(\boldsymbol{x}) = \left\{1, x, y, x^2, xy, y^2\right\};\ m = 6, \tag{5}$$

The polynomial basis has to satisfy an extra requirement in order to obtain an unique solution [51]:

$$\sum_{i=1}^{n} p_j(\boldsymbol{x}_i) a_i(\boldsymbol{x}_i) = 0,\ j = 1, 2, \ldots, m. \tag{6}$$

in which n represents the number of nodes inside the influence-cell of interest point $\boldsymbol{x}_I$. Therefore, applying Eqs. (1) and (6) to every node forming the influence-cell of interest point $\boldsymbol{x}_I$, a new equation system can be written,

$$\begin{Bmatrix} \boldsymbol{u}_s \\ \boldsymbol{0} \end{Bmatrix} = \begin{bmatrix} \boldsymbol{R}_Q & \boldsymbol{P}_m \\ \boldsymbol{P}_m^T & \boldsymbol{0} \end{bmatrix} \begin{Bmatrix} \boldsymbol{a} \\ \boldsymbol{b} \end{Bmatrix} = \boldsymbol{G} \begin{Bmatrix} \boldsymbol{a} \\ \boldsymbol{b} \end{Bmatrix} \tag{7}$$

where $\boldsymbol{u}_s$ are the variable values at the nodes inside the influence-cell of interest point $\boldsymbol{x}_I$. It must be noted that the geometric matrix $\boldsymbol{G}$ is a symmetric matrix because the distance is directional independent, i.e., $R(r_{ij}) = R(r_{ji})$. By solving Eq. (7) and substituting its solution into Eq. (1), the shape function $\boldsymbol{\phi}(\boldsymbol{x}_I)$ is obtained,

$$\begin{aligned} \left\{\boldsymbol{\varphi}(\boldsymbol{x}_I), \boldsymbol{\psi}(\boldsymbol{x}_I)\right\} = \left\{\boldsymbol{R}^T(\boldsymbol{x}_I), \boldsymbol{p}^T(\boldsymbol{x}_I)\right\}\boldsymbol{G}^{-1} = \big\{\{\varphi_1(\boldsymbol{x}_1), \varphi_2(\boldsymbol{x}_2), \ldots, \\ \varphi_n(\boldsymbol{x}_1)\}, \{\psi_1(\boldsymbol{x}_1), \psi_2(\boldsymbol{x}_2), \ldots, \psi_m(\boldsymbol{x}_1)\}\big\} \end{aligned} \tag{8}$$

Notice, that the shape function $\boldsymbol{\phi}(\boldsymbol{x}_I)$ is only formed by the first n terms, $\{\phi_1(\boldsymbol{x}_1), \phi_2(\boldsymbol{x}_2), \ldots, \phi_n(\boldsymbol{x}_1)\}$. The last m terms $\{\psi_1(\boldsymbol{x}_1), \psi_2(\boldsymbol{x}_2), \ldots, \psi_m(\boldsymbol{x}_1)\}$ are not included in the shape function vector because they are a by-product of Eq. (8), with no relevant physical meaning associated [10].

Previous works on the RPI [48,49] ensured that the unity partition is verified and, moreover, that these shape functions possess the delta Kronecker property, which simplify the imposition of the essential and natural boundary conditions. The NNRPIM formulation is described with detail in [10].

In this work, both the NNRPIM formulation considering first degree influence cells (NNRPIMv1) and second degree influence cells (NNRPIMv2) were used to solve the numerical examples.

3. Free vibration analysis and matrix formulation

Consider a solid with a domain Ω bounded by Γ. In the absence damping effects, the dynamic equilibrium based on the principle of virtual work can be written as

$$\int_{\Omega} \delta\boldsymbol{\varepsilon}^{\mathrm{T}} \boldsymbol{\sigma} d\Omega + \int_{\Omega} \delta\boldsymbol{u}^{\mathrm{T}} \rho \ddot{\boldsymbol{u}} d\Omega + \int_{\Omega} \delta\boldsymbol{u}^{\mathrm{T}} \boldsymbol{b} d\Omega - \int_{\Gamma_t} \delta\boldsymbol{u}^{\mathrm{T}} \boldsymbol{t} d\Gamma = 0 \tag{9}$$

where $\boldsymbol{u}$ and $\ddot{\boldsymbol{u}}$ are, respectively, the displacement and the acceleration field, $\boldsymbol{b}$ is the body force vector and $\boldsymbol{t}$ the traction on the natural boundary, Γ_t. The strain vector $\boldsymbol{\varepsilon}$ is defined as

$$\boldsymbol{\varepsilon} = \boldsymbol{L}\,\boldsymbol{u} \tag{10}$$

where $\boldsymbol{L}$ is the differential operator defined in Eq. (11):

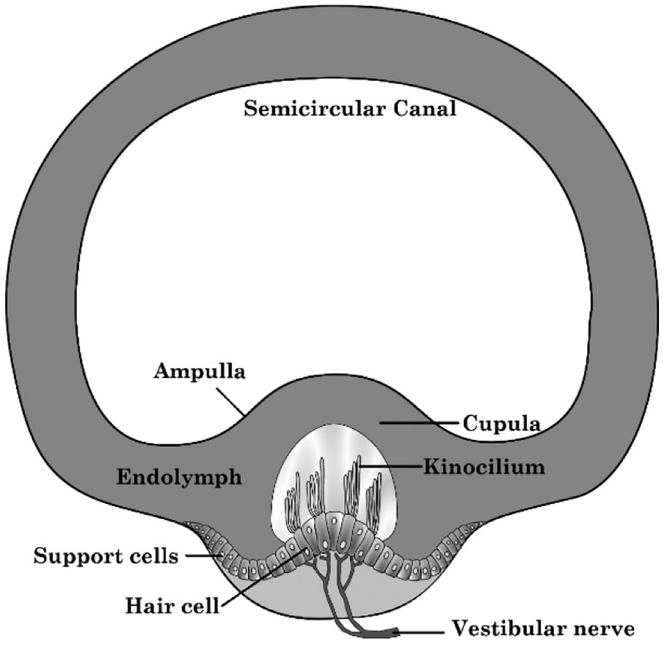

Fig. 2. Scheme of one SCC of the inner ear with the cupula.

$$\boldsymbol{L} = \begin{bmatrix} \frac{\partial}{\partial x} & 0 & 0 & \frac{\partial}{\partial y} & 0 & \frac{\partial}{\partial z} \\ 0 & \frac{\partial}{\partial y} & 0 & \frac{\partial}{\partial x} & \frac{\partial}{\partial z} & 0 \\ 0 & 0 & \frac{\partial}{\partial z} & 0 & \frac{\partial}{\partial y} & \frac{\partial}{\partial x} \end{bmatrix}^T \tag{11}$$

The linear constitutive relations can be given by

$$\boldsymbol{\sigma} = \boldsymbol{c}\boldsymbol{\varepsilon} \tag{12}$$

Being $\boldsymbol{\sigma}$ the stress tensor and $\boldsymbol{c}$ the material matrix defined as

$$\boldsymbol{c} = \mu_1 \begin{bmatrix} 1 & \nu & \nu & 0 & 0 & 0 \\ \nu & 1 & \nu & 0 & 0 & 0 \\ \nu & \nu & 1 & 0 & 0 & 0 \\ 0 & 0 & 0 & \mu_2 & 0 & 0 \\ 0 & 0 & 0 & 0 & \mu_2 & 0 \\ 0 & 0 & 0 & 0 & 0 & \mu_2 \end{bmatrix} \tag{13}$$

being $\mu_1 = E/(1-\nu^2)$ and $\mu_2 = E/(2+2\nu)$, where E is the Young's modulus and ν is the Poisson's ratio. In general, the first term of Eq. (9) can be presented as

$$\int_\Omega \delta\boldsymbol{\varepsilon}^{\mathrm{T}}\boldsymbol{\sigma}d\Omega = \delta\boldsymbol{u}\left[\int_\Omega \boldsymbol{B}^T\boldsymbol{c}\boldsymbol{B}d\Omega\right]\boldsymbol{u} \tag{14}$$

The second term of Eq. (9) can be developed as

$$\int_\Omega \delta\mathbf{u}^{\mathrm{T}}\rho\,\ddot{\boldsymbol{u}}d\Omega = \int_\Omega \delta(\boldsymbol{H}\boldsymbol{u})^T\rho(\boldsymbol{H}\ddot{\boldsymbol{u}})d\Omega = \delta\boldsymbol{u}\left[\int_\Omega \boldsymbol{H}^T\rho\boldsymbol{H}d\Omega\right]\ddot{\boldsymbol{u}} \tag{15}$$

where $\boldsymbol{B}$ is the deformation matrix, defined in Eq. (16), $\boldsymbol{H}$ is the interpolation function diagonal matrix, $\boldsymbol{H}_I = \boldsymbol{\phi}(\boldsymbol{x}_I)\boldsymbol{I}$, and ρ is defined with $\boldsymbol{\rho} = \rho\boldsymbol{I}$, being ρ the mass density of the material and $\boldsymbol{I}$ the identity matrix with size 3 × 3. Thus, the stiffness matrix can be defined as: $\boldsymbol{K} = \int_\Omega \boldsymbol{B}^T\boldsymbol{c}\boldsymbol{B}d\Omega$, and the mass matrix as: $\boldsymbol{M} = \int_\Omega \boldsymbol{H}^T\boldsymbol{\rho}\boldsymbol{H}d\Omega$.

$$\boldsymbol{B}(\boldsymbol{x}_I)_i^T = \begin{bmatrix} \frac{\partial\varphi_i}{\partial x} & 0 & 0 & \frac{\partial\varphi_i}{\partial y} & 0 & \frac{\partial\varphi_i}{\partial z} \\ 0 & \frac{\partial\varphi_i}{\partial y} & 0 & \frac{\partial\varphi_i}{\partial x} & \frac{\partial\varphi_i}{\partial z} & 0 \\ 0 & 0 & \frac{\partial\varphi_i}{\partial z} & 0 & \frac{\partial\varphi_i}{\partial y} & \frac{\partial\varphi_i}{\partial x} \end{bmatrix} \tag{16}$$

The force vectors are defined by developing the third and fourth terms of Eq. (9),

$$\boldsymbol{F}_t = \int_{\Gamma_t} \boldsymbol{H}^T t d\Gamma_t \;\; and \;\; \boldsymbol{F}_b = \int_\Omega \boldsymbol{H}^T\boldsymbol{b}d\Omega \tag{17}$$

Both vectors can be combined, $\boldsymbol{F} = \boldsymbol{F}_t + \boldsymbol{F}_b$. The essential boundary conditions can be directly imposed in the mass matrix and in the stiffness matrix as in the FEM, since the NNRPIM interpolation function possesses the delta Kronecker property. Thus, the equilibrium equations governing the linear dynamic response, neglecting the damping effect, can be represented in the matrix form

$$\boldsymbol{M}\ddot{\boldsymbol{U}} + \boldsymbol{K}\boldsymbol{U} = \boldsymbol{F} \tag{18}$$

where $\boldsymbol{U} = \boldsymbol{u}$ and $\ddot{\boldsymbol{U}} = \ddot{\boldsymbol{u}}$. The fundamental mathematical method used to solve Eq. (18) is the separation of variables. This approach [52] assumes that the solution can be expressed in the following form:

$$\boldsymbol{U}(t) = \Phi\boldsymbol{X}(t) \tag{19}$$

where Φ is an $n_{3D} \times n_{3D}$ square matrix containing m spatial vectors independent of the time variable t, $\boldsymbol{X}(t)$ is a time dependent vector, and $n_{3D} = 3N$ for the 3D formulation, being N the total number of nodes in the problem domain. The components of $\boldsymbol{X}(t)$ are called generalized displacements. From Eq. (19) it follows that $\ddot{U}(t) = \Phi\ddot{\boldsymbol{X}}(t)$. It is required that the space functions satisfy the following stiffness and mass orthogonality conditions:

$$\Phi^T\boldsymbol{K}\Phi = \Omega \quad \text{and} \quad \Phi^T\boldsymbol{M}\Phi = \boldsymbol{I} \tag{20}$$

where Ω is the diagonal matrix which contains the free vibration frequencies, ω_i^2. After substituting Eq. (20) and its derivatives in order to time into Eq. (18) and pre-multiplying it by Φ^T, the equilibrium equation that corresponds to the modal generalized displacement is obtained. The solution can be presented in the form,

$$\boldsymbol{u}(t) = \phi\sin\left(\omega\left(t - t_0\right)\right) \tag{21}$$

being $\boldsymbol{\phi}$ the vector of order n_{3D}, t the time variable, the constant initial time is defined by t_0 and ω is the vibration frequency vector. Substituting the former solution into Eq. (22) the generalized eigenproblem is obtain, from which $\boldsymbol{\phi}$ and ω must be determined,

$$\boldsymbol{K}\phi = \omega^2\boldsymbol{M}\phi \tag{22}$$

Eq. (22) yields the n_{3D} eigensolutions:

$$\begin{cases} \boldsymbol{K}\phi_1 = {\omega_1}^2\boldsymbol{M}\phi_1 \\ \boldsymbol{K}\phi_2 = {\omega_2}^2\boldsymbol{M}\phi_2 \\ \vdots \\ \boldsymbol{K}\phi_{n_{3D}} = {\omega_{n_{3D}}}^2\boldsymbol{M}\phi_{n_{3D}} \end{cases} \tag{23}$$

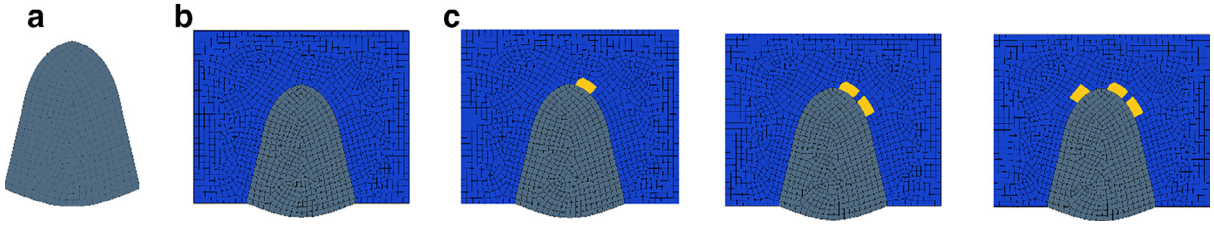

Fig. 3. Two dimensional model; (a) Cupula; (b) Cupula with endolymph; (c) Cupula with endolymph and otoconia placed in different location.

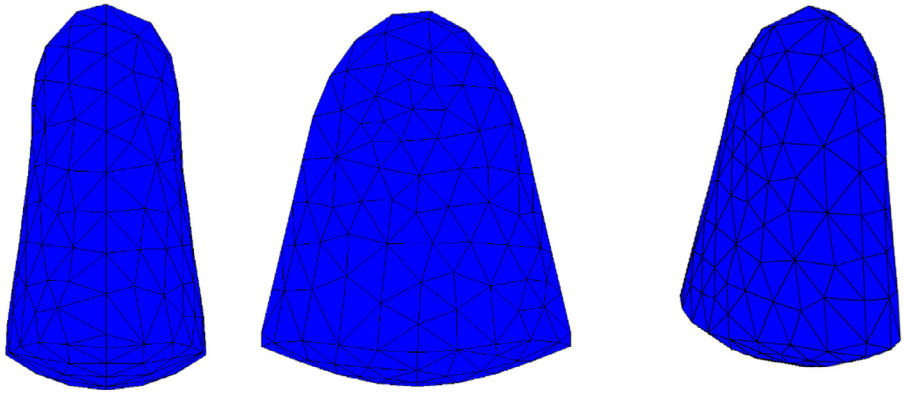

Fig. 4. Three-dimensional finite element model of the cupula, front, lateral and three-dimensional views.

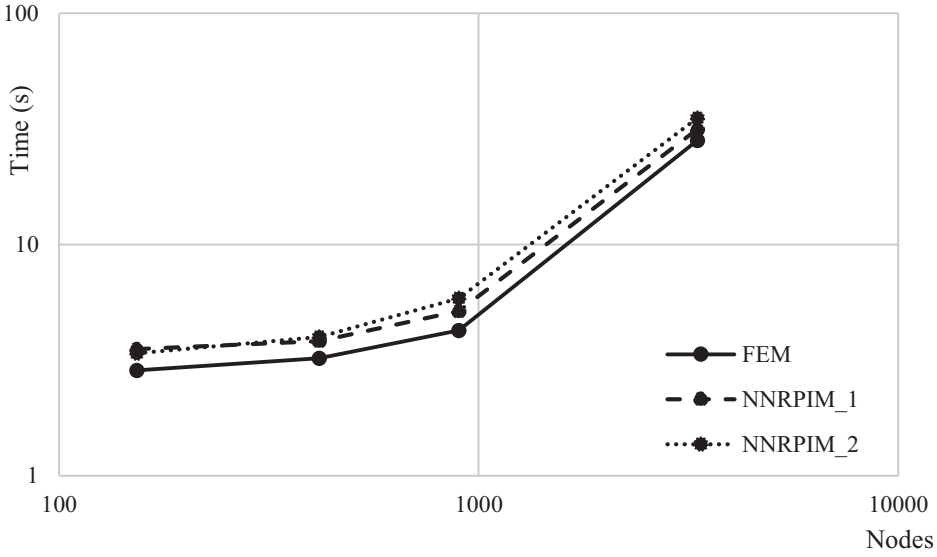

Fig. 5. Computational cost for the three methodologies used.

The vector ϕ_i is called the ith mode shape vector and ω_i is the corresponding vibration frequency. Defining a matrix $\mathbf{\Phi}$ whose columns are the eigenvectors ϕ_i,

$$\mathbf{\Phi} = \begin{bmatrix} \phi_1 & \phi_2 & \cdots & \phi_{n_{3D}} \end{bmatrix} \tag{24}$$

and a diagonal matrix $\mathbf{W}$ which stores the eigenvalues ω_i,

$$\mathbf{W} = \begin{bmatrix} {\omega_1}^2 & 0 & \cdots & 0 \\ 0 & {\omega_2}^2 & \cdots & 0 \\ \vdots & \vdots & \ddots & \vdots \\ 0 & 0 & \cdots & {\omega_{n_{3D}}}^2 \end{bmatrix} \tag{25}$$

the n_{3D} solutions can be written as:

$$\boldsymbol{K\Phi} = \mathbf{M}\,\mathbf{\Phi}\,\mathbf{W} \tag{26}$$

It is required that the space functions satisfy the following stiffness and mass orthogonality conditions:

$$\mathbf{\Phi}^T \boldsymbol{K\Phi} = \mathbf{W} \tag{27}$$

and

$$\mathbf{\Phi}^T \boldsymbol{M\Phi} = \boldsymbol{I} \tag{28}$$

After substituting Eq. (19) and its time derivatives into Eq. (18) and pre-multiplying by $\mathbf{\Phi}^T$, the equilibrium equation that corresponds to the modal generalized displacement is obtained.

4. Numerical application

There are two sensory parts of the vestibular system of the inner ear that promote the body balance: the sacs, where particles called otoconia originally located, and the three semicircular canals (SCC), containing the cupula (Fig. 2).

The cupula is a gelatinous hydromechanical sensor that transforms mechanical movement into electrical signals, which are then sent to the brain. The movement of the cupula is induced by the endolymph during the body motion [53,54]. There are many diseases affecting the vestibular system, most of them lead to vertigo, which is the most common symptom in older people. Since vertigo episodes lead to a false sense of rotation (which can cause nausea and vomiting), it is important to avoid that kind of symptoms, which in a severe case could cause a fall [55].

Benign paroxysmal positional vertigo (BPPV) is one of the most common diseases causing vertigo [56]. One particular case of BPPV is cupulolithiasis, which occurs when the otoconia get lost in the SCC and attach to the cupula, inducing a false sensation of movement and leading to vertigo [57]. In this work, the modal generalized displacements of the cupula will be calculated in order to obtain the natural frequency of the cupula and understand the mechanical implications of the attachment otoconia to the cupula.

In order to obtain numerically the free vibration modes of the cupula, 2D and 3D discrete models were built using the standard dimensions and the approximated mechanical properties found in the literature [58].

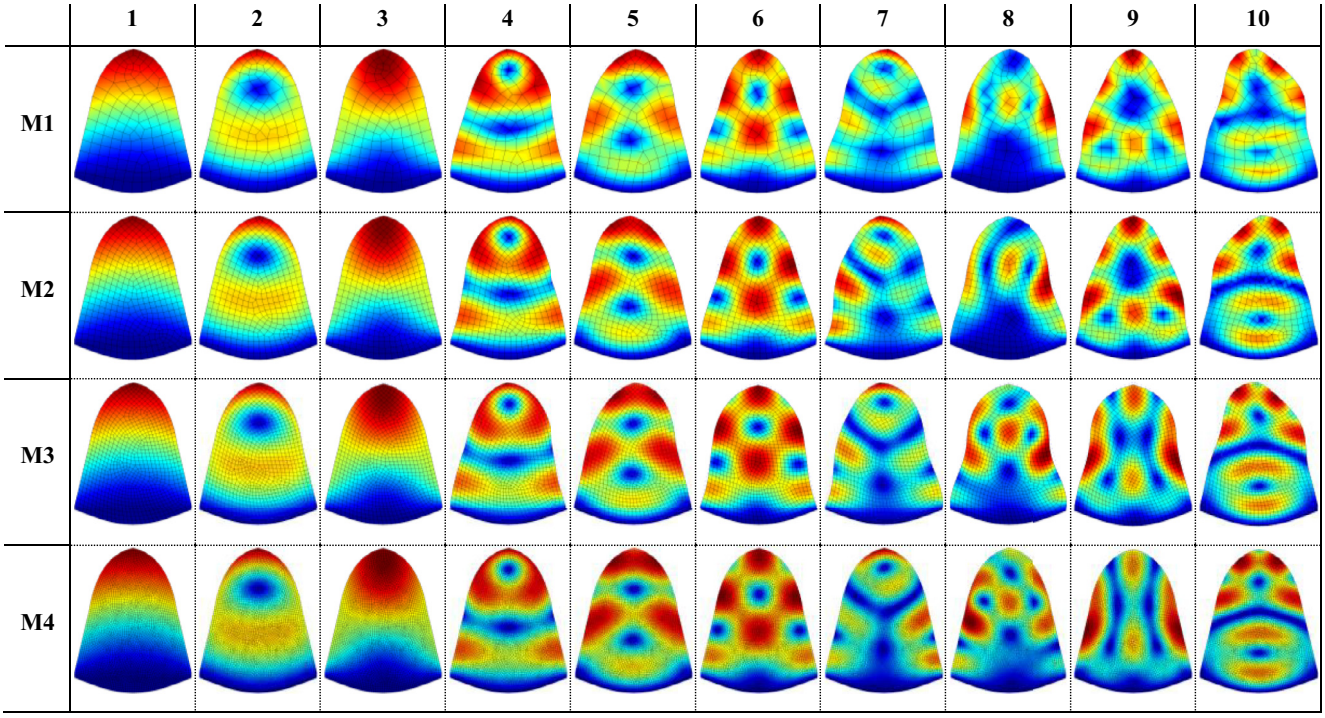

Fig. 6. Ten first modes of the two-dimensional cupula with FEM, four meshes. (For interpretation of the references to colour in the text, the reader is referred to the web version of this article.)

4.1. Numerical model

First it is presented the 2D model of the cupula (Fig. 3a) that was constructed using quadratic elements. Four different meshes were built: M1 (153 nodes, 131 elements), M2 (417 nodes, 382 elements), M3 (897 nodes, 846 elements) and M4 (3320 nodes, 3221 elements). The endolymph around the cupula was also simulated (Fig. 3b). Regarding the cupulolithiasis, three different simulations were performed with otoconia placed in different location around the cupula (Fig. 3c).

Moreover, a 3D model of the cupula was built using tetrahedral elements (Fig. 4). Thus, four different meshes were built: M1 (350 nodes, 1461 elements), M2 (692 nodes, 3156 elements), M3 (1151 nodes, 5453 elements) and M4 (2128 nodes, 10,704 elements).

Regarding the material properties for the cupula, it was considered the following: $E = 5 \times 10^{-6}$ MPa, $\upsilon = 0.49$ and $\rho = 1 \times 10^{-9}$ ton/mm^3 for all simulations. In the case of the otoconia material (calcium carbonate crystals), the properties used are $E = 6.6$ MPa, $\upsilon = 0.45$ and $\rho = 2.4 \times 10^{-9}$ ton/mm^3 [58]. To simulate the endolymph, the properties considered are $\rho = 1 \times 10^{-9}$ ton/mm^3 $\upsilon = 0.49$ and $E = 1.27 \times 10^{-7}$ MPa. Notice that the endolymph is an incompressible highly viscous fluid, with a dynamic viscosity, $\mu = 0.000852$ Pa s. It was verified (in this work) that the natural frequency of the cupula is around 50 Hz, which means that its period of vibration is $T = 1/50$ s. Thus, knowing that $\dot{\tau} = \mu\dot{\gamma}$ and $\tau = G\gamma$, it is possible to instantaneously approximate the distortion modulus G with $G \cong \mu/T \cong 0.0426$ Pa (valid for the first vibration mode). Thus, since $G = E/(2 + 2\nu)$, then $E = 0.127$ Pa.

Regarding the essential boundary conditions, in the 2D and 3D models of the cupula without surrounding fluid, the nodes at the cupula's base are constrained in all its degrees of freedom (no movement is allowed on those nodes). For the 2D models considering the surrounding endolymph, all the boundaries of the model are fully constrained.

5. Results

In this section, the results obtained with the simulations performed with FEM and NNRPIM formulations are presented. The results include the vibration modes and frequencies of the cupula (2D and 3D), the cupula surrounded by the endolymph and also with attached otoconias. The 2D analysis was performed considering the plane strain assumptions and the 3D analysis was performed assuming the formulation presented in Section 3. In this work, the 2D finite element analyses are performed using the standard 2D four nodes quadrilateral element, and the 3D finite element studies are executed considering the standard 3D four nodes constant strain tetrahedron elements [6].

5.1. Computational cost

In order to understand the computational efficiency of the NNRPIM, the 2D four nodal meshes previously mentioned (M1, M2, M3 and M4) were analyzed using the FEM and the first degree influence cell NNRPIM formulation (NNRPIMv1) and the second degree influence-cell NNRPIM formulation (NNRPIMv2). It is important to mention that the authors have programed their own NNRPIM and FEM codes, and that all theirs routines were written and analyzed within Matlab© environment. Additionally, the computer used to analyze the problem is an Intel i7 Quad-Core processor, running at 3.6 GHz with 16 GB RAM.

The computational cost of each analysis is plotted in Fig. 5. It is possible to visualize that although the three numerical methods show a similar computational cost, the FEM shows slightly lower computational cost when compared with the NNRPIMv1 and NNRPIMv2. This result was expected, since the FEM obtains the shape-functions using less nodes than the NNRPIM formulation leading, as a consequence, to narrower banded stiffness matrices. Notice that constructing shape functions with a lower number of nodes reduces the computational cost (but decreases also the accuracy of the approximation) and inverting narrower banded stiffness matrices is less time consuming that inverting sparse or broader banded stiffness matrices [10].

5.2. Cupula (2D)

The first ten vibration modes of the cupula obtained with the FEM using the four different meshes (M1 to M4) are presented in Fig. 6. In order to visualize automatically both the shape of the vibration mode and

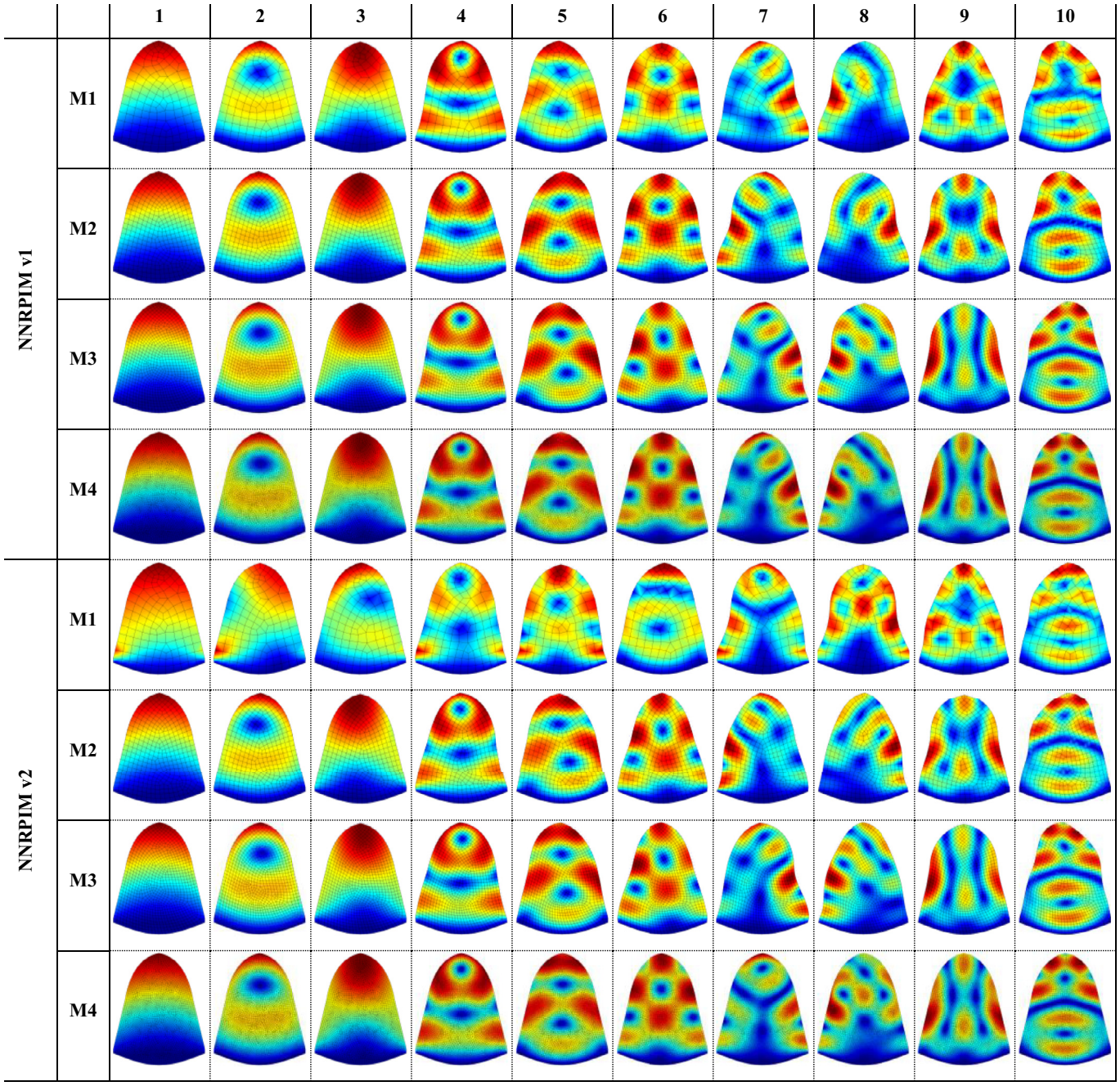

Fig. 7. Ten first modes of the two-dimensional cupula with NNRPIM, four meshes.

the vibration frequency, the results of the figures correspond to a fictitious displacement field obtained with: $\boldsymbol{U}_i = \omega_i \varphi_i$. With this visualization technique, it is possible to visualize in each figure the corresponding magnitude of the vibration frequency by observing the maximum value of the displacement, designated by the red color; since the blue color corresponds to the lower displacement values.

Concerning the NNRPIMv1 and NNRPIMv2 analyses, the results of the four different meshes of the cupula are shown in Fig. 7. Additionally, in Table 1 the magnitudes of the first ten vibration frequencies of the analyzed model of the cupula are presented.

In the first and fifth lines of the Fig. 7, corresponding to mesh M1, it is possible to observe that the solution obtained has not yet stabilized. This effect is confirmed analyzing the vibration frequencies of the same modes in Table 1, which are the lower values compared with the natural frequencies of the other meshes. This result is expected, since at this stage (for mesh M1) the solution has not yet converged. All the other meshes (M2, M3 and M4) and modes (1–10) in the NNRPIM analyses show similar values compared with the equivalent results obtained with FEM (Fig. 6).

As Table 1 shows, the FEM and NNRPIMv1 formulations possess a monotonic convergence path. Notice that the values obtained for the less discretized meshes are monotonically evolving to the ones obtained with the most discretized meshes. In opposition, the NNRPIMv2 formulation appears to achieve the convergence very fast. Although the NNRPIMv2 results obtained with M1 are always very different from the ones obtain with M4, it is possible to visualize that the solution obtained with M2 has already converged, being the results obtained with M2, M3 and M4 almost identical. Furthermore, the final converged results are all very close, regardless the used numerical formulation. The results indicate that first vibration frequency is between 51.71 Hz and 53.43 Hz.

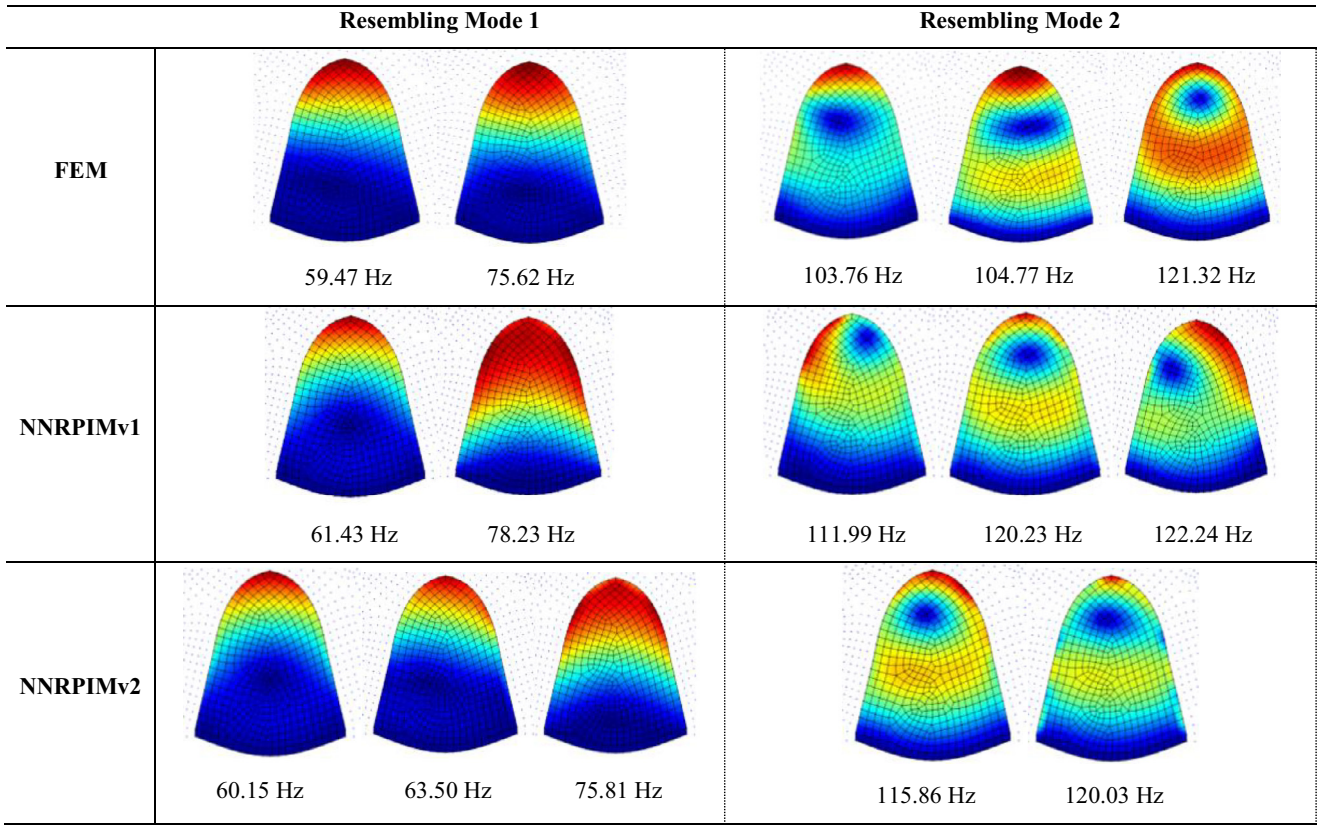

Fig. 8. Two first modes of the two-dimensional cupula with endolymph using FEM and NNRPIMv1 and NNRPIMv2.

Table 1
Natural frequency of ten first modes of the two-dimensional cupula with FEM and NNRPIM (four meshes).

	Natural Frequency (Hz)											
	FEM				NNRPIMv1				NNRPIMv2			
	M1	M2	M3	M4	M1	M2	M3	M4	M1	M2	M3	M4
1	57.17	54.70	54.84	53.13	53.43	54.31	53.00	52.60	23.39	51.48	51.87	51.71
2	127.08	121.32	119.84	117.88	122.89	119.47	117.19	117.68	103.06	117.36	116.21	117.16
3	135.86	131.62	131.39	128.90	129.69	130.33	128.50	128.05	111.82	126.35	126.80	126.68
4	239.55	226.17	222.55	217.48	223.77	219.22	216.13	215.97	187.38	213.64	213.61	214.17
5	277.15	259.80	254.56	248.80	262.23	254.47	249.71	247.98	234.57	249.12	247.89	247.21
6	283.32	265.13	259.03	253.34	265.31	257.03	254.11	251.25	252.32	251.08	251.63	249.60
7	369.27	345.26	337.34	328.04	336.22	331.44	329.11	325.23	301.68	321.02	323.82	322.11
8	382.59	350.33	340.87	331.17	343.12	336.73	331.48	327.71	316.98	330.41	329.03	324.83
9	404.24	362.51	350.08	340.07	373.02	346.85	340.13	337.80	344.12	338.08	337.23	336.35
10	428.11	386.60	372.53	360.07	390.57	371.30	360.63	357.57	367.15	361.29	357.06	356.37

Additionally, notice that the following vibration frequencies are much higher, which allow to identify with enough precision the magnitude of frequency of the first mode.

All the natural frequencies obtained are contained in the human hearing range, since it goes from 20 Hz to 20,000 Hz. In general, the natural frequencies obtained with NNRPIM are lower than the ones obtained with FEM.

5.3. Cupula with endolymph (2D)

In this subsection, the endolymph is included in the model (Fig. 3b). The objective is to understand the influence of the endolymph in the natural frequency (the first vibration frequency) of the cupula.

Since in the previous section it was verified that the mesh density of mesh M2 is sufficient to obtain accurate results, in this section a similar mesh density is used to discretize the problem domain.

Thus, in order to observe the effect of the endolymph around the cupula, the first five vibration modes of the cupula are presented in the Fig. 8, for the FEM and both NNRPIM analyses, respectively.

Notice that the first two vibration modes obtained with the FEM resemble the first vibration mode obtained in Section 5.2. Furthermore, the third, fourth and fifth vibration modes obtained now are very similar with the second vibration mode obtained in the analysis of the cupula without surrounding fluid (Section 5.2).

The same effect is verified for the NNRPIM, the first three vibration modes of the present analysis resemble the first vibration mode obtained in Section 5.2 and the fourth and fifth vibration modes of the present analysis are very similar with the second vibration mode obtained in Section 5.2.

Regarding the first vibration modes (resembling the natural frequency of the isolated cupula), in this study the following vibration frequencies were obtained: 59 Hz and 75 Hz in FEM, 61 Hz and 78 Hz

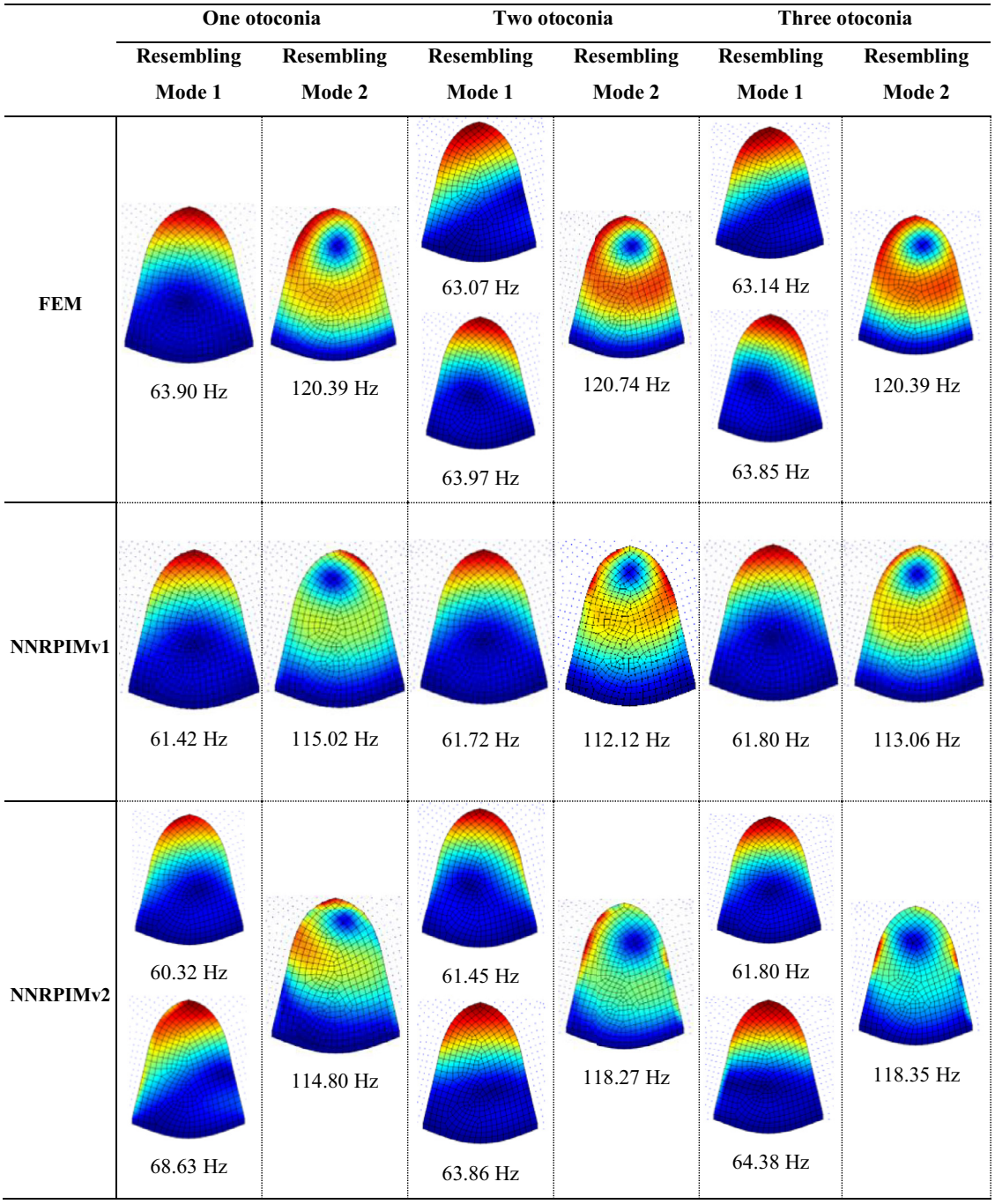

Fig. 9. Two first modes of the two-dimensional cupula with endolymph and otoconia using FEM and NNRPIM.

for the NNRPIMv1 analysis and 60 Hz, 63 Hz, and 76 Hz in NNRPIMv2 analysis. Notice that these values are very close with the ones observed in Section 5.2, indicating that the fluid has a reduced influence in the magnitude of the cupula's natural frequency.

5.4. Cupula with endolymph and otoconia (2D)

Next, the 2D problem shown in Fig. 3c is analyzed with both FEM and NNRPIM formulations. Here, groups of otoconia are attached to the cupula in different locations (the three locations shown in Fig. 3c), simulating a possible cause for vertigo. With this study it is intended to understand if the inclusion of the otoconia changes significantly the natural frequency of the cupula. In this study, in addition to the otoconia, the surrounding fluid is also considered. Again, the density of the discretization used in this study follows the mesh density of mesh M2 presented in Section 4.

The relevant vibration modes obtained, and the corresponding vibration frequencies are presented in Fig. 9.

Fig. 9 shows that the FEM and the NNRPIM produce always very similar vibration modes. It is possible to visualize that vibration modes resembling the first vibration mode found in Section 5.2 present a vibration frequency very close with the one found in Section 5.2.

When one otoconia (or one otoconia group) is considered, the frequencies of the cupula resembling its natural frequency (observed in Section 5.2) are 63.90 Hz in the FEM, 61.42 Hz for the NNRPIMv1, and 60.32 Hz or 68.63 Hz in the NNRPIMv2.

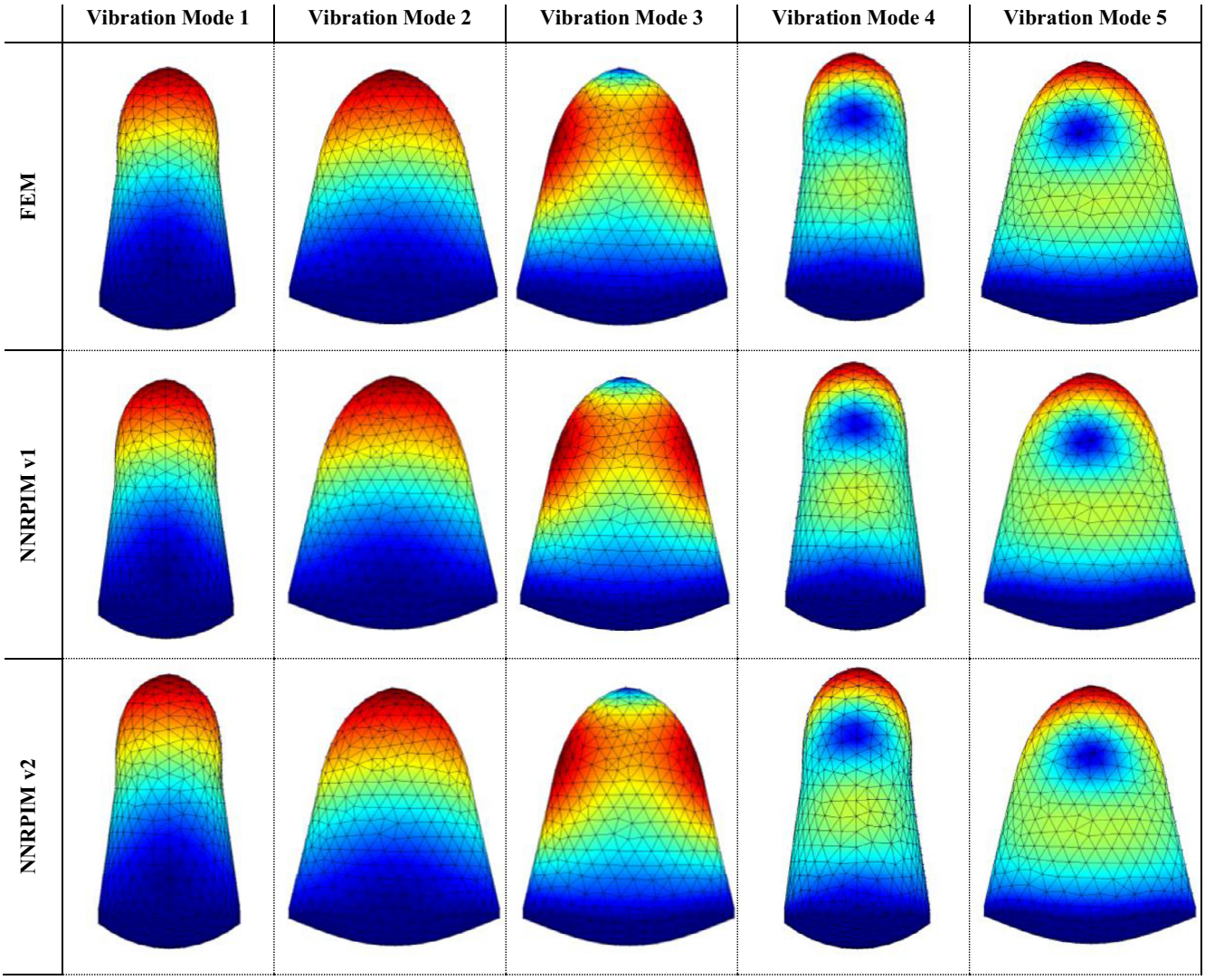

Fig. 10. Five first modes of the three-dimensional cupula with FEM, NNRPIMv1 and NNRPIMv2.

Alternatively, if two otoconia (or two otoconia groups) are considered, the frequencies of the cupula resembling its natural frequency (Section 5.2) are 63.07 Hz or 63.97 Hz for the FEM. 61.72 Hz for the NNRPIMv1, and 61.45 Hz or 63.86 Hz for the NNRPIMv2.

If three otoconia (or three otoconia groups) are attached to the cupula, the frequencies resembling its natural frequency, documented in Section 5.2, are 63.14 Hz or 63.85 Hz for the FEM, 61.80 Hz for the NNRPIMv1, and 61.80 Hz or 64.38 Hz for the NNRPIMv2.

Regarding the apparent second vibration mode obtained with the models with one and two otoconia, from both methods (FEM and NNRPIM), is it possible to observe a small fictitious displacement of the cupula to the right side comparing with the model with three otoconia, resembling more with the model without otoconia. This trend behavior could be justified with the placement of the otoconia in the right side of the cupula in the two first examples. This result is more evident in the NNRPIM.

On the other hand, the first vibration frequencies obtained from the models with the different number of otoconia are very close between each other. This may indicate that the size of the otoconia particles is not enough to change significantly the vibration frequency of the cupula. Although the FEM and NNRPIM formulations show similar results, the natural frequencies obtained with FEM continue to be higher than the ones obtained with the NNRPIMv1 and NNRPIMv2 formulations.

5.5. Cupula (3D)

Expectably, the analysis of the free vibration modes of the 3D cupula will allow to understand in a more realistic way the behavior of the cupula. The free vibration analysis of the 3D cupula is performed with the four meshes shown in Section 4. Nevertheless, in the Fig. 10 are presented only the results obtained with mesh M4 for the first five vibration modes of the cupula with FEM and NNRPIM. The first and fourth modes are represented with the lateral view, the other ones with the front view.

Since the second mode of vibration in the three-dimensional analysis shows a fictitious displacement aligned with the tangent direction of the canal, this second mode of vibration should be the most suitable to induce the necessary movement to restore the otoconia back to the right place.

Table 2 shows the first vibration frequencies obtained for the cupula using the distinct four meshes and the FEM and NNRPIM analysis. It is possible to visualize that both the NNRPIM formulations present high convergence rates. Notice that the solution obtained for meshes M2, M3 and M4 is almost identical. On the other hand, the FEM presents a lower convergence rate. This was expected, since the literature shows that the tetrahedral element possesses lower convergence rates [6].

As already mentioned, the 3D second vibration mode corresponds to the vibration configuration aligned with the tangent direction of the canal. Thus, the 3D second vibration mode corresponds to the 2D first

Numerical technique a	b		2D analysis vibration modes $i=1$	$i=2$	$i=3$	3D analysis vibration mode $i=1$	$i=2$	$i=3$
FEM	NNRPIM v1	$\xi_i^{a/b}\times 100$	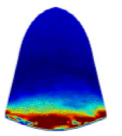	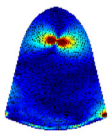	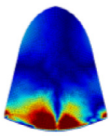	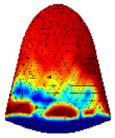	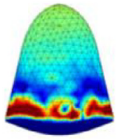	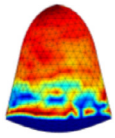
		$\bar{\xi}_i^{a/b}\times 100$	3.10%	1.57%	2.82%	12.26%	9.91%	7.60%
FEM	NNRPIM v2	$\xi_i^{a/b}\times 100$	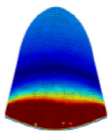	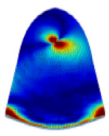	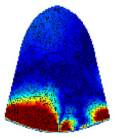	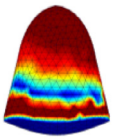	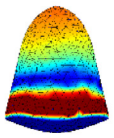	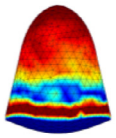
		$\bar{\xi}_i^{a/b}\times 100$	11.4%	2.11%	3.60%	22.03%	20.97%	9.95%
NNRPIM v1	FEM	$\xi_i^{a/b}\times 100$	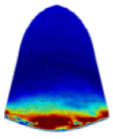	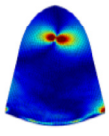	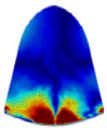	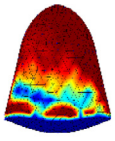	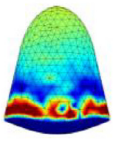	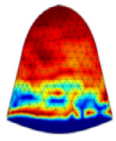
		$\bar{\xi}_i^{a/b}\times 100$	2.7%	1.57%	2.78%	11.48%	8.21%	8.87%
NNRPIM v1	NNRPIM v2	$\xi_i^{a/b}\times 100$	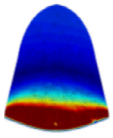	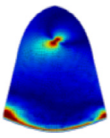	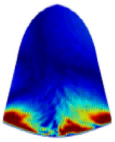	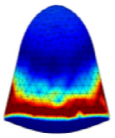	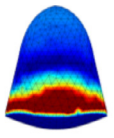	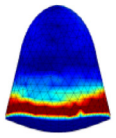
		$\bar{\xi}_i^{a/b}\times 100$	7.5%	1.68%	2.38%	11.70%	13. 30%	5.42%
NNRPIM v2	FEM	$\xi_i^{a/b}\times 100$	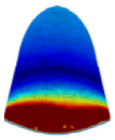	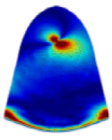	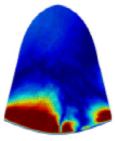	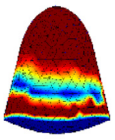	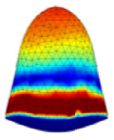	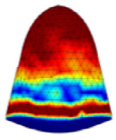
		$\bar{\xi}_i^{a/b}\times 100$	9.6%	2.05%	3.20%	15.48%	13.29%	10.55%
NNRPIM v2	NNRPIM v1	$\xi_i^{a/b}\times 100$	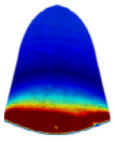	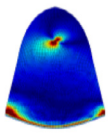	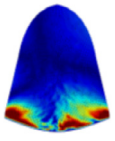	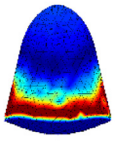	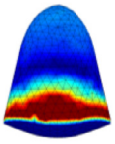	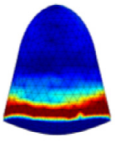
		$\bar{\xi}_i^{a/b}\times 100$	7.1%	1.62%	2.19%	8.98%	9.27%	4.71%
			0%		>10%			

Fig. 11. Distribution maps $\xi(\boldsymbol{x})_i^{a/b}$ and corresponding average differences $\bar{\xi}_i^{a/b}$.

Table 2
Natural frequency of five first modes of the three-dimensional cupula with FEM and NNRPIM (four meshes).

	Natural Frequency (Hz)											
	FEM				NNRPIMv1				NNRPIMv2			
	M1	M2	M3	M4	M1	M2	M3	M4	M1	M2	M3	M4
1	52.33	47.04	46.23	43.97	43.69	41.07	40.91	39.94	35.48	40.17	40.02	39.21
2	62.75	58.62	57.40	56.14	56.29	54.11	54.06	53.09	41.97	52.18	52.77	51.91
3	108.99	99.83	95.30	90.77	87.86	85.07	84.29	82.98	86.30	84.04	83.32	82.11
4	144.55	133.47	130.67	124.58	122.64	117.02	116.52	114.49	111.42	114.78	114.55	112.07
5	146.43	136.42	134.26	130.85	129.19	126.18	126.37	124.99	118.75	124.55	125.09	123.41

vibration mode. From Table 2 it is possible to visualize that for the densest mesh (M4), the FEM predicts a second vibration frequency of 56.14 Hz, the NNRPIMv1 predicts 53.09 Hz and the NNRPIMv2 indicates 51.91 Hz. These values are in accordance with the one obtained in the 2D analysis.

5.6. Cross-comparison

In order to compare the several formulations, a cross-comparison was performed. Thus, for the 2D analysis, the first three vibration modes obtained in Section 5.2 with the FEM and NNRPIM formulations, using mesh M4, were compared with each other. The cross-comparison was performed with the following described procedure. In the end of each analysis the first three vibration frequencies and corresponding vibration modes are obtained. The vibration mode of a solid represents the typical final configuration charactering how the solid vibrates when excited with the corresponding vibration frequency. Therefore, as already mentioned in Section 3, the vector representing the ith vibration mode is defined as φ_i. Notice that φ_i is the $[2N \times 1]$ array defining the typical final configuration characterizing how the solid vibrates when excited with the ith vibration frequency (recall that N is the total number of nodes discretizing the problem domain). In order to perform a cross-comparison, the following expression is applied to each node discretizing the problem domain. For instances, for node $\boldsymbol{x}_j$:

$$\xi(\boldsymbol{x}_j)_i^{a/b} = \frac{\phi(\boldsymbol{x}_j)_i^a - \phi(\boldsymbol{x}_j)_i^b}{\phi(\boldsymbol{x}_j)_i^b} \tag{29}$$

being a a numerical formulation (for example, FEM) and b another numerical formulation (for example, NNRPIMv1). In the end, a new distribution map representing the relative differences between technique a and b, will be obtained, $\xi(\boldsymbol{x})_i^{a/b}$, for each ith vibration frequency.

In the end, after obtaining all the three $\xi(\boldsymbol{x})_1^{a/b}$, $\xi(\boldsymbol{x})_2^{a/b}$ and $\xi(\boldsymbol{x})_3^{a/b}$ distributing maps (corresponding to the first, second and third vibration frequencies, respectively), a global average difference between techniques a and b was calculated:

$$\bar{\xi}_i^{a/b} = \frac{1}{N}\sum_{j=1}^{N} \xi(\boldsymbol{x}_j)_i^{a/b} \tag{30}$$

The same technique was applied to the 3D analysis. Thus, once again, the first three vibration modes obtained in Section 5.5 with the FEM and NNRPIM formulations, using mesh M4, were used to perform the comparisons.

Following this technique, several difference distribution maps $\xi(\boldsymbol{x})_i^{a/b}$ were obtained and several average differences $\bar{\xi}_i^{a/b}$ were calculated.

Fig. 11 shows the difference distribution maps, $\xi(\boldsymbol{x})_i^{a/b}$, and corresponding average differences, $\bar{\xi}_i^{a/b}$, obtained for the three first vibration modes of the 2D and 3D cupula with the FEM and NNRPIM analysis using the mesh M4. In Fig. 11 only differences below 10% are shown. This will allow to understand clearly the extent of domain in which the differences are higher than 10%.

In the 2D analysis, it is possible to visualize that the FEM and the NNRPIMv1 formulation allow to obtain close results. Alternatively, the NNRPIMv2 solution presents higher differences when compared with the FEM solutions. However, the NNRPIMv1 and the NNRPIMv2 produce very close results.

Notice that the NNRPIMv1 formulation only uses first degree influence cells. Therefore, commonly, each influence cell is formed with 3–9 nodes. On the other hand, the NNRPIMv2 uses the second degree influence cells, which means that each influence cell could be formed with 9–27 nodes (commonly). Regarding the FEM, the quadratic element used in the 2D analysis possesses 4 nodes in each element. As it is possible to understand, the quadratic element formulation is much closer to the NNRPIMv1 formulation than to the NNRPIMv2 formulation. Thus, it is natural that the difference between the FEM solution and the NNRPIMv1 solution is smaller than the difference between the FEM and the NNRPIMv2. These results do not conclude about the best numerical formulation, they only permit to understand the magnitude of their differences.

The same observations can be found for the 3D analysis. Nevertheless, in the 3D analysis the difference between the formulations are much higher. For the 3D analyses, only the comparison between the NNRPIMv2 and NNRPIMv1 allows to obtain global average differences below 10%. Once again, the differences between the NNRPIMv1 and the FEM solutions are smaller than the ones found between the NNRPIMv2 and the FEM results.

Another relevant observation from Fig. 11 is the fact that differences for the first vibration mode are higher in almost cases comparing with the differences found for the second and third vibration modes.

6. Conclusion

In this work, the FEM and the NNRPIM were used to analyze numerically the dynamic response of the cupula. The results show that both techniques are capable to achieve similar results. However, most importantly, this work opens a new research branch in the computational analysis of the vestibular system.

As Table 1 shows, for the 2D analysis, the FEM and NNRPIMv1 formulations possess a solid convergence. The values obtained for the less discretized mesh (M1) are monotonically evolving to the ones obtained with the most discretized mesh (M4). On the other hand, the NNRPIMv2 formulation appears to achieve the convergence extremely soon. Notice that for M2 the solution has already converged, being the results obtained with M2, M3 and M4 almost identical.

Concerning the results of the 3D analysis, both the NNRPIM formulations present high convergence rates (Table 2). The solution obtained for meshes M2, M3 and M4 is almost identical. In opposition, the FEM appears to present lower convergence rates. This can be explained with the kind of element used in the finite element analysis—tetrahedral element, which possesses a low convergence rate.

Furthermore, the final converged results are all very close, regardless the used numerical formulation. The 2D results indicate that first vibration frequency is between 51.71 Hz and 53.43 Hz for the 2D analysis. Additionally, the 3D results for the same vibration mode (which in 3D is the second vibration mode) indicate a similar vibration frequency between 51.91 Hz and 56.14 Hz. Furthermore, if only the NNRPIMv2 results are considered, the resemblance is much closer: 51.71 Hz (2D) and 51.91 Hz (3D).

The results from Tables 1 and 2 show that the target vibration frequency of the cupula (corresponding the first vibration mode in 2D and the second vibration mode in 3D) present a very distinct value (around 52–56 Hz) when compared with the vibration frequencies of other vibration modes. This is an advantage, it means that it will be possible to easily identify the target vibration frequency of the cupula.

The dynamic response of a structure strongly depends on its geometric shape, material properties and environment, as confirmed by the results obtained in this work. The response of the cupula when it is surrounded by endolymph (and also with attached otoconia particles) present different natural frequencies, as Fig. 8 shows. Nevertheless, the first vibration frequencies are between 59.47 Hz and 61.43 Hz. These magnitudes are close to the ones obtained without the surrounding endolymph (51.71 Hz and 53.43 Hz).

This result is relevant. It means that a simulation in which the surrounding endolymph is disregard will allow to obtain a satisfactory approximated solution.

Another very important conclusion concerns the inclusion (or not) of otoconia in the model. As Fig. 9 shows, it was found that the inclusion of otoconia do not modify (significantly) the vibration frequency of the cupula. Notice that the first vibration frequency of the cupula with surrounding endolymph and without otoconia is between 59.47 Hz and 61.43 Hz (Fig. 8) and the same first vibration frequency of the cupula

with surrounding endolymph and with otoconia is between 60.32 Hz and 63.90 Hz (Fig. 9-1 otoconia); 61.45 Hz and 63.07 Hz (Fig. 9-2 otoconia); and 61.80 Hz and 63.85 Hz (Fig. 9-3 otoconia).

In this work, the distinct formulations are directly compared by means of a computational cost study and a cross-comparison study. It was found that the FEM formulation presents a slightly lower computational cost when compared with the NNRPIM formulations. However, notice that the NNRPIMv2 formulation converges very fast. Actually, in 2D, for mesh M2, the NNRPIMv2 formulation is already capable to produce results very close with its final converged solution (M4). On the other hand, the FEM presents a more slow convergence rate. Thus, comparing the computational cost of a 2D analysis using NNRPIMv2 and mesh M2 and the computational cost of a 2D analysis using FEM and mesh M4, it is visible that FEM will present a higher computational cost.

Regarding the cross-comparison study, it was possible to observe that both NNRPIM formulations allow to obtain very similar results, regardless the spatial dimension of the analysis (2D or 3D). Additionally, it was found that the FEM solution is closer with the NNRPIMv1 solutions rather the NNRPIMv2 solution. This observation (more evident in the 2D analysis) can be explained with the number of nodes used to construct the shape functions.

Since one particular case of BPPV is cupulolithiasis, (the attachment of otoconia to the cupula), this research work will allow in the future some new therapeutic solutions based on the induction of the cupula vibration by means of a sound source. With this work, it was possible to understand that the natural frequency of the cupula ranges between 51 Hz or 61 Hz and all the other vibration frequencies possess very distinct values. Since theoretically, the resonance phenomena will force the cupula to vibrate, the induced vibration will allow to detach the otoconia particles from the cupula, reducing the vertigo symptoms. This could be achieve with non-invasive way, such as listening to music with a predominant set of bass sounds.

Acknowledgments

The authors acknowledge the funding by Ministério da Ciência, Tecnologia e Ensino Superior—Fundação para a Ciência e a Tecnologia, Portugal and POCH—Programa Operacional Capital Humano, comparticipado pelo Fundo Social Europeu e por fundos nacionais do MCTES under research grants SFRH/BD/108292/2015, SFRH/BPD/111020/2015, IF/00159/2014 and by project funding MIT-EXPL/ISF/0084/2017 and UID/EMS/50022/2013 (funding provided by the inter-institutional projects from LAETA).

Additionally, the authors gratefully acknowledge the funding of Project NORTE-01-0145-FEDER-000022—SciTech—Science and Technology for Competitive and Sustainable Industries, cofinanced by Programa Operacional Regional do Norte (NORTE2020), through Fundo Europeu de Desenvolvimento Regional (FEDER).

References

[1] Jaeger R, Takagi A, Haslwanter T. Modeling the relation between head orientations and otolith responses in humans. Hear. Res. Nov. 2002;173(1–2):29–42.
[2] Duncan RK, Grant JW. A finite-element model of inner ear hair bundle micromechanics. Hear. Res. Feb. 1997;104(1–2):15–26.
[3] Grieser B, Obrist D. “Validation of assumptions on the endolymph motion inside the semicircular canals of the inner ear,” Internal reports of the Institute of Fluid Dynamics. ETH Zurich, pp. 1–16, 2012.
[4] Kassemi M, Deserranno D, Oas JG. Fluid–structural interactions in the inner ear. Comput. Struct. Jan. 2005;83(2–3):181–9.
[5] Kondrachuk A. Finite element modeling of the 3D otolith structure. J. Vestib. Res. Jan. 2001;11(1):13–32.
[6] Liu G-R, Quek SS. The finite element method : a practical course. 2nd ed. Butterworth-Heinemann; 2013.
[7] Nguyen VP, Rabczuk T, Bordas S, Duflot M. Meshless methods: a review and computer implementation aspects. Math. Comput. Simul. Dec. 2008;79(3):763–813.
[8] Belytschko PKT, Krongauz Y, Organ D, Fleming M. Meshless methods: an overview and recent developments. Comput. Methods Appl. Mech. Eng. Dec. 1996;139(1–4):3–47.
[9] Gu YT. Meshfree methods and their comparisons. Int. J. Comput. Methods Dec. 2005;2(4):477–515.
[10] Belinha J. Meshless methods in biomechanics—bone tissue remodelling analysis. Tavares JMRS, Natal Jorge RM, editors. Switzerland: Springer International Publishing; 2014.
[11] Belinha J, Araújo AL, Ferreira AJM, Dinis LMJS, Natal Jorge RM. The analysis of laminated plates using distinct advanced discretization meshless techniques. Compos. Struct. May 2016;143:165–79.
[12] Dinis LMJS, Natal Jorge R, Belinha J. Analysis of 3D solids using the natural neighbour radial point interpolation method. Comput. Methods Appl. Mech. Eng. Mar. 2007;196(13–16):2009–28.
[13] Belinha J, Dinis LMJS, Natal Jorge RM. The natural radial element method. Int. J. Numer. Methods Eng. Mar. 2013;93(12):1286–313.
[14] Sukumar N, Moran B, Belytschko T. The natural element method in solid mechanics. Int. J. Numer. Methods Eng. Nov. 1998;43(5):839–87.
[15] Sukumar N, Moran B, Yu Semenov A, Belikov VV. Natural neighbour Galerkin methods. Int. J. Numer. Methods Eng. Jan. 2001;50(1):1–27.
[16] Ferreira AJM. A formulation of the multiquadric radial basis function method for the analysis of laminated composite plates. Compos. Struct. Feb. 2003;59(3):385–92.
[17] Doblaré M, Cueto E, Calvo B, Martínez MA, Garcia JM, Cegoñino J. On the employ of meshless methods in biomechanics. Comput. Methods Appl. Mech. Eng. Feb. 2005;194(6–8):801–21.
[18] Wong KCL, Wang L, Zhang H, Liu H, Shi P. Meshfree implementation of individualized active cardiac dynamics. Comput. Med. Imaging Graph. Jan. 2010;34(1):91–103.
[19] Chen G, et al. A new approach for assigning bone material properties from CT images into finite element models. J. Biomech. Mar. 2010;43(5):1011–15.
[20] Do T, Khosravifard A, Hematiyan MR, Bui TQ. Accurate and efficient analysis of stationary and propagating crack problems by meshless methods. Theor. Appl. Fract. Mech. Feb. 2017;87:21–34.
[21] Bui TQ, Vu T-V, Nguyen N-H, Khosravifard A, Hematiyan MR, Tanaka S. A simple FSDT-based meshfree method for analysis of functionally graded plates. Eng. Anal. Bound. Elem. Jun. 2017;79:1–12.
[22] Bui TQ, Nguyen MN, Zhang C, Pham DAK. An efficient meshfree method for analysis of two-dimensional piezoelectric structures. Smart Mater. Struct. Jun. 2011;20(6):65016.
[23] Bui TQ, Tanaka S, Suzuki H, Sadamoto S, Imachi M. Analysis of cracked shear deformable plates by an effective meshfree plate formulation. Eng. Fract. Mech. Aug. 2015;144:142–57.
[24] Zhang C, Bui TQ, Nguyen MN. Buckling analysis of Reissner–Mindlin plates subjected to in-plane edge loads using a shear-locking-free and meshfree method. Eng. Anal. Bound. Elem. Sep. 2011;35(9):1038–53.
[25] Sadamoto S, Ozdemir M, Tanaka S, Taniguchi K, Yu TT, Bui TQ. An effective meshfree reproducing kernel method for buckling analysis of cylindrical shells with and without cutouts. Comput. Mech. Jun. 2017;59(6):919–32.
[26] Yanagihara D, Sadamoto S, Tanaka S, Taniguchi K, Ozdemir M, Bui TQ, Murakami C. Buckling analysis of stiffened plate structures by an improved meshfree flat shell formulation. Thin Walled Struct. Aug. 2017;117:303–13.
[27] Nguyen MN, Bui TQ. A moving Kriging interpolation-based meshfree method for free vibration analysis of Kirchhoff plates. Comput. Struct. Feb. 2011;89(3–4):380–94.
[28] Bui TQ, Nguyen MN, Zhang C. An efficient meshfree method for vibration analysis of laminated composite plates. Comput. Mech. Aug. 2011;48(2):175–93.
[29] Zhang C, Bui TQ, Nguyen MN. A meshfree model without shear-locking for free vibration analysis of first-order shear deformable plates. Eng. Struct. Dec. 2011;33(12):3364–80.
[30] Golub M, Bui TQ, Khosravifard A, Zhang C, Hematiyan MR. Dynamic analysis of sandwich beams with functionally graded core using a truly meshfree radial point interpolation method. Eng. Struct. Feb. 2013;47:90–104.
[31] ElZahab AJKZ, Divo E. A localized collocation meshless method (LCMM) for incompressible flows CFD modeling with applications to transient hemodynamics. Eng. Anal. Bound. Elem. Aug. 2009;33(8–9):1045–61.
[32] Ho AK, Tsou L, Green S, Fels S. A 3D swallowing simulation using smoothed particle hydrodynamics. Comput. Methods Biomech. Biomed. Eng. Imaging Vis. Oct. 2014;2(4):237–44.
[33] Gámiz MJ, Lopez-Escamez JA. Health-related quality of life in patients over sixty years old with benign paroxysmal positional vertigo. Gerontology Feb. 2004;50(2):82–6.
[34] Santos CF, Belinha J, Gentil F, Parente M, Jorge RN. An alternative 3D numerical method to study the biomechanical behaviour of the human inner ear semicircular canal. Acta Bioeng. Biomech. 2017;19(1):3–15.
[35] Dinis LMJS, Natal Jorge RM, Belinha J. A natural neighbour meshless method with a 3D shell-like approach in the dynamic analysis of thin 3D structures. Thin Walled Struct Jan. 2011;49(1):185–96.
[36] Sibson R. A brief description of natural neighbor interpolation, vol. 4. Chichester, New York: Wiley; 1981.
[37] Sibson R. A vector identity for the Dirichlet tessellation. Math. Proc. Camb. Phil. Soc. 1980;87:151–5.
[38] Voronoi GM. Nouvelles applications des parame‘tres continus a‘ la the´orie des formes quadratiques. Deuxie‘me Me´moire: Recherches sur les paralle´lloe‘dres primitifs. Reine Angew. Math 1908;134:198–287.
[39] Delaunay B. Sur la sphe´re vide. A la memoire de Georges Voronoı. Izv. Akad. Nauk SSSR, Otd. Mat. i Estestv. Nauk. 1934(6):793–800.
[40] Belytschko T, Lu YY, Gu L. Element-free Galerkin methods. Int. J. Numer. Methods Eng. Jan. 1994;37(2):229–56.
[41] Liu WK, Jun S, Li S, Adee J, Belytschko T. Reproducing kernel particle methods for structural dynamics. Int. J. Numer. Methods Eng. May 1995;38(10):1655–79.

[42] Atluri SN, Zhu T. A new meshless local Petrov–Galerkin (MLPG) approach in computational mechanics. Comput. Mech. Aug. 1998;22(2):117–27.
[43] Liu GR, Gu YT. A point interpolation method for two-dimensional solids. Int. J. Numer. Methods Eng. Feb. 2001;50(4):937–51.
[44] Li Y, Dai KY, Liu GR, Han X. Inelastic analysis of 2D solids using a weak–form RPIM based on deformation theory. Comput. Methods Appl. Mech. Eng. Jul. 2006;195(33–36):4179–93.
[45] Hematiyan MR, Khosravifard A, Bui TQ. Efficient evaluation of weakly/strongly singular domain integrals in the BEM using a singular nodal integration method. Eng. Anal. Bound. Elem. Apr. 2013;37(4):691–8.
[46] Racz D, Bui TQ. Novel adaptive meshfree integration techniques in meshless methods. Int. J. Numer. Methods Eng. Jun. 2012;90(11):1414–34.
[47] Tanaka S, Suzuki H, Sadamoto S, Sannomaru S, Yu T, Bui TQ. J-integral evaluation for 2D mixed-mode crack problems employing a meshfree stabilized conforming nodal integration method. Comput. Mech. Aug. 2016;58(2):185–98.
[48] Wang JG, Liu GR. A point interpolation meshless method based on radial basis functions. Int. J. Numer. Methods Eng. Aug. 2002;54(11):1623–48.
[49] Liu GR, Wang JG. On the optimal shape parameters of radial basis functions used for 2-D meshless methods. Comput. Methods Appl. Mech. Eng. Mar. 2002;191(23–24):2611–30.
[50] Hardy RL. Theory and applications of the multiquadric-biharmonic method 20 years of discovery 1968–1988. Comput. Math. Appl. Jan. 1990;19(8–9):163–208.
[51] Bowman H, Golberg MA, Chen CS. Some recent results and proposals for the use of radial basis functions in the BEM. Eng. Anal. Bound. Elem. Apr. 1999;23(4):285–96.
[52] Bathe K-J. Finite element procedures. 2nd ed. Englewood Cliffs: Prentice-Hall; 1996.
[53] Winter DA. Human balance and posture control during standing and walking. Gait & Posture 1995;3(4):193–214.
[54] Diener HC, Dichgans J. On the role of vestibular, visual and somatosensory information for dynamic postural control in humans. Prog. Brain Res. 1988;76:253–62.
[55] Taylor J, Goodkin HP. Dizziness and vertigo in the adolescent. Otolaryngol. Clin. North Am. Apr. 2011;44(2):309–21 vii–viii.
[56] Karatas M. Central vertigo and dizziness. Neurologist Nov. 2008;14(6):355–64.
[57] Squires TM, Weidman MS, Hain TC, Stone HA. A mathematical model for top-shelf vertigo: the role of sedimenting otoconia in BPPV. J. Biomech. Aug. 2004;37(8):1137–46.
[58] Davis JL, Xue J, Peterson EH, Grant JW. Layer thickness and curvature effects on otoconial membrane deformation in the utricle of the red-ear slider turtle: static and modal analysis. J. Vestib. Res. 2007;17(4):145–62.